



# Electroadsorption of $\text{La}^{3+}$ and $\text{Ce}^{3+}$ from aqueous media with a carbon paste electrode modified with HMS-CMPO

Carlos Díaz<sup>a,b</sup>, Mauricio Gómez<sup>b</sup>, Alicia Matta<sup>b</sup>, Jaime Pizarro<sup>b,\*</sup>

<sup>a</sup> Instituto de Ciencias, Universidad de Las Américas, Sede Providencia, Manuel Montt 948, Santiago, Chile

<sup>b</sup> Departamento de Ingeniería Geoespacial y Ambiental, Facultad de Ingeniería, Universidad de Santiago de Chile, Santiago, Chile

## ARTICLE INFO

### Keywords:

Cerium  
Carbamoyl methyl phosphine oxide  
Electroadsorption  
Lanthanum  
Mesoporous materials  
Modified electrode

## ABSTRACT

This work deals with the electroadsorption of rare earths cerium and lanthanum in aqueous solution by using a carbon paste electrode modified with a silica mesoporous material functionalized with carbamoyl methyl phosphine oxide (CMPO). This functionalization was carried out in a two-step synthesis, the intermediate product was synthesized by attaching N-(2-aminoethyl)-3-aminopropyltrimethoxysilane (APTMS) to the surface of the HMS by a grafting method synthesis, then this intermediate was modified by CMPO, in a further condensation reaction. The final product CMPO obtained was characterized by diffuse reflectance infrared Fourier transform spectroscopy (DRIFTS), thermal gravimetric analysis (TGA) and  $\text{N}_2$  adsorption/desorption isotherms using BJH and BET models. Showing thermal stability, a surface area higher than  $450\text{m}^2\text{g}^{-1}$  and mesoporous properties. The CMPO material was used to modify the mixture of the carbon paste electrode producing an enhancement in the interaction between the electrode surface and the lanthanides studied, at the same time it produces and improvement in the electroactive area by over two orders of magnitude. The modified carbon paste electrode (CMPO-CPE) developed in this work shows an increase in the conductivity, observed with the electrochemical impedance spectroscopy studies, and an increase in the electroactive area of 47 % was calculated from cyclic voltammetry experiments. CMPO-CPE was used to extract  $\text{La}^{3+}$  and  $\text{Ce}^{3+}$  from aqueous solution using  $\text{NaNO}_3$  as support electrolyte, by using a fixed potential program over time, measuring the obtained current by Chronoamperometric method. The adsorption and desorption results were corroborated with Inductively coupled plasma atomic emission spectroscopy (ICP-OES) demonstrated the capacity of extraction of the electrode were  $74\ \mu\text{g}$  after ten cycles for  $\text{La}^{3+}$  at pH 5.0 and  $15\ \mu\text{g}$  after ten cycles for  $\text{Ce}^{3+}$  at pH 6.0, using a CMPO modified electrode of small surface (3 mm radius). This electrode was tested for over 50 cycles without losing their electroactive properties under tested electrochemical conditions.

## 1. Introduction

Climate change has brought many challenges, one of them being how governments are to develop their economies. Since is not such an option for different industries to offshore of the environmental problems, environmentally friendly technologies must be considered within their strategies. Technologies such as electromobility, low-to-zero carbon emission processes, sustainable energy production, among others are included among the potential solutions [1–5].

High-tech developments have led to demand for rare earth elements (REE), as Lanthanum and Cerium, for example, have many applications in optical glasses, flat screens, low-energy light bulbs, catalyst in petroleum refining industry, NiMH batteries, superconductors, magnets,

alloys for electromobility, scintillators, torches, and polishing powder [6–9].

Lanthanides are associated with two main sources, the primary one is associated with minerals such as basnasite, monazite and xenotime, where its high affinity for oxygen is associated with the formation of oxides. The secondary source is related to the extraction of these elements from products at the end of their useful life (permanent magnets, fluorescent lamps, batteries, cathode tubes, and others) [10–12]. Both sources of lanthanides are obtained mainly by a leaching process, followed by a solvent extraction process [6,9,13].

Several separation methods stand out in the literature, such as coprecipitation, liquid-liquid extraction, ion exchange, HPLC high-pressure chromatography and adsorption. The adsorption process

\* Corresponding author.

E-mail addresses: [jaime.pizarro@usach.cl](mailto:jaime.pizarro@usach.cl), [jpizarrok@gmail.com](mailto:jpizarrok@gmail.com) (J. Pizarro).

<https://doi.org/10.1016/j.micromeso.2024.113248>

Received 27 September 2023; Received in revised form 1 July 2024; Accepted 2 July 2024

Available online 3 July 2024

1387-1811/© 2024 Published by Elsevier Inc.

mainly uses ion exchange polymers, silica gel and nanoparticles as adsorbents; the range of adsorbents highlights the great potential as an adsorption method; however, the method has low selectivity, limited adsorption capacity, and presents difficulties when large volumes of solution are used [14–21].

Lanthanides have a common capacity to stable form trivalent ion aqueous acidic media, with very close ionic radii [22,23], they are hard cations, they interact with hard anions such as hydroxides, alkoxides, carbonates and phosphates, and form complexes with organic ligands containing carboxylates and phosphonates [24,25]. The speciation of  $\text{La}^{3+}$  and  $\text{Ce}^{3+}$  complexes in aqueous solution are pH dependent; where under acidic environment, are free cationic species and at alkaline pH they tend to form hydroxides [26,27].

Nowadays, the challenge has been to replace them with more environmentally friendly methods with high extraction efficiency [28]. The use of electrochemical processes such as electroadsorption or capacitive deionization is of increasing interest since it facilitates the removal of low concentration metal ions from aqueous solutions, these methods are easily scalable and may be introduced in the refinement process due to their modular nature [29–33]. The use of working electrodes made of carbonous materials has been increased latest years. Those electrodes may enhance the surface of the electrode and may be chemically modified to enhance selectivity as well [34–37].

The development of electrochemical methods to offer less time-consuming processes and the advances in the design of carbonous electrodes allows the development of task specific devices with relative low cost, high sensitivity, and selectivity with a low background current [38]. Some of the applications for these devices are in analytical chemistry [39,40], environmental remediation [41,42] and for electroadsorption of heavy metals [43–45].

Carbon paste electrodes (CPE) are a suitable device for the study of silica based mesoporous material due to the high reproducibility of the electrode, easy to modify and the easily renewal surface [38–40,42,46,47]. The electrochemical study of the addition of these new solid materials to the paste mixture is appropriated to evaluate enhancement in catalytic properties, surface area, selectivity, and sensitivity of the electrodes [46–49].

This manuscript presents the use of a mix of graphite powder with hexagonal mesoporous silica (HMS) material functionalized with carbamoyl methyl phosphine oxide (CMPO) moieties [50], such functional groups have been used before to design solvents for REE extraction, the effect of the HMS-CMPO in the electroadsorption of  $\text{La}^{3+}$  and  $\text{Ce}^{3+}$  will be reviewed in this work.

## 2. Experimental

### 2.1. Raw materials and reagents

Dodecylamine (DDA >98 %), N-(2-aminoethyl)-3-aminopropyltrimethoxysilane (APTMS >97 %), diethylphosphonoacetic acid (>95 %) and 1,1 carbonyldiimidazole (CDI >90 %) were all purchased from Sigma Aldrich. Tetraethyl orthosilicate (TEOS >99 %), 1,3,5-trimethylbenzene (TMB >97 %), sodium hydroxide (>98 %), dimethylformamide (DMF >99.5 %), ethanol (>99.9 %), 2-propanol (>99 %), were all purchased from Merck.

### 2.2. Hexagonal mesoporous silica (HMS) synthesis

The HMS material was obtained via the method reported previously [51]. 1.5 g of DDA was pour into a 250 mL beaker, and then dissolved in 100.0 mL of a mixture ethanol: water 1:1.5 %v/v at room temperature and stirred until homogeneity. Afterwards, 0.64g of TEOS were added to the mixture, the solutions turn blurry, and then rapidly 0.8 g of TMB were added to act as spacer in the development of the mesoporous material. The pH of the resulting mixture was adjusted until 9.0, by adding NaOH 1 M under 500 RPM stirring, and keep stirring by 24 h

until HMS precipitated. Next, the precipitated obtained was filtered with MN 616 cellulose filter and washed with cold water and let dry in a desiccator overnight for further use and characterization.

### 2.3. Synthesis of intermediate HMS-APTMS

1.1g of the previously synthesized starting material, HMS, were pour into a 250 mL ballon flask, then 4 mmol of APTMS and 50 mL of toluene were added to the ballon flask and let to reflux over 24 h. The precipitated obtained was filtered with MN 616 cellulose filter and washed with 2-propanol five times and left to dry overnight, in a drying oven at 333K, then was also stored in desiccator to be used and characterized later.

### 2.4. Synthesis of HMS-CMPO

The dry intermediated product HMS-APTMS was pour within 250 mL ballon flask with 60 mL of DMF under Ar atmosphere, then 7 mmol of CDI and 3 mmol of diethylphosphonoacetic acid were added to the mixture and stirred over 12 h until the final material HMS-CMPO was obtained. The product was filtered with MN 616 cellulose filter and rinsed with five times with cold water, 2 propanol, and acetone, and then storage to let dry by 48 h inside a desiccator before use and characterization.

### 2.5. Physicochemical and morphological characterization of HMS and its derivatives

The characterization of the HMS and its derivatives was made by a Diffuse reflectance infrared Fourier transform spectrometer (DRIFTS), using a Spectrum Two FT-IR Spectrometer (PerkinElmer) using steel rods, at room temperature. Thermogravimetric Analysis (TGA) were performed with a Mettler Toledo Gas Controller GC20 Stare System TGA/DSC, using STARE software. The temperature ramp used was from 303 to 873K, the temperature rate was 20 °C per minute, under a  $\text{N}_2$  flux of 20 mL per minute. The porosity of the HMS and its derivativities were analyzed by  $\text{N}_2$  adsorption-desorption isotherms, performed at 77 K using a 3Flex gas analyser (Micromeritics); total pore volume was determined at  $p/p_0 = 0.99$ , average pore size was determined from the method of Barrett, Joyner, and Halenda (BJH) and surface area was measured using Brunauer, Emmet, and Teller (BET) method. Crystalline structure of the mesoporous materials synthesized were followed by small angle X ray scattering. (SAXS). These measurements were carried out using the SAXSpoint 2.0 instrument by Anton Paar, at low angle 2 $\theta$  from 0.5° to 4° at 0.12° s<sup>-1</sup> in this range. The system is equipped with a Primux 100 micro microfocus X-ray source using Cu K $\alpha$  monochromatic radiation ( $\lambda = 0.154$  nm) in high-resolution mode with a sample-to-detector distance of 530 mm.

### 2.6. Electrode preparation

Modified carbon paste electrodes were prepared by adding 0–20 % w/w of HMS-CMPO to 70–50 %w/w of graphite powder (Merck), then mixing with 2 mL of diethyl ether until homogeneity into an agate mortar, ether was eliminated by evaporation to obtain the solid mixture and let dry at 333K oven overnight to evaporate all ether residues. Carbon paste electrodes were prepared by mixing 70 %w/w of solid mixture with 30%w/w of paraffin oil (Sigma Aldrich) in agate mortar [52]. The resulting mixture paste was placed into a Teflon tube, using stainless steel as electrical contact, for further electrochemical characterization.

### 2.7. Electrochemical characterization

All electrochemical experiments were performed using a Palm Sense electrochemical working station, model PS Trace 4. Cyclic Voltammetry, Linear Sweep Voltammetry Chronoamperometric and Electrochemical

Impedance Spectrometry experiments were performed using a one chamber glass cells. The Carbon Paste Electrodes were used as working electrode, Ag/AgCl and SCE electrode (CH Instruments) were used as reference electrodes. Pt wire (CH Instruments) was used as counter electrodes, all electrochemical experiments were run out under Ar atmosphere and under ambient temperature 298K.

## 2.8. Electroadsorption/desorption study

Electroadsorption method was carried out by Chronoamperometric measurements in a one chamber electrochemical cell using a three electrodes arrangement, under Ar atmosphere over 200 s per cycle. Ag/AgCl electrode was used as reference and Pt wire was used as counter electrode. The electroadsorption potential and pH conditions were fixed at  $-0.6V$  and pH 5.0 for  $Ce^{3+}$ ; and  $-0.3V$  and pH 6.0 for  $La^{3+}$  respectively. After the species were deposited over the surface of the carbon paste working electrode it was rinsed with deionized water to remove the excess of the electroadsorption solution.

Then the working electrode was introduced into a second one chamber glass cell, where another Ag/AgCl electrode was used as reference electrode, also another Pt wire was used as counter electrode. The desorption cycle lasted 200 s and was run out under Ar atmosphere. In this case also for both  $Ce^{3+}$  and  $La^{3+}$  fixed desorption potential and pH applied were 0.8V and pH 2.0. In both cases the electroadsorption/desorption cycles were repeated five times, conductivity of the desorption solution was measured after every desorption cycle, and then the concentration of  $Ce^{3+}$  and  $La^{3+}$  present in the solution, after the five cycles, were measured by ICP-OES to corroborate the conductivity results.

## 3. Results and discussion

### 3.1. Synthesis of HMS-CMPO

The synthesis of the products was conducted following the method described before by Pizarro et al. [50], and detailed in the experimental section. The functionalization of the hexagonal mesoporous siliceous (HMS) material was carried out in two steps, starting with the reaction of the N-(2-aminoethyl)-3-aminopropyltrimethoxysilane (APTMS) with the hydroxyl moieties over the surface of the HMS material, forming the intermediate (HMS-APTMS) which have primary amine functional groups, over the surface of the material, necessary for the further grafting reaction. The HMS-APTMS was rather used to be grafted with the 1,1 carbonyl-diimidazole (CDI) and the diethyl-phosphonoacetic acid to form the final product HMS-CMPO. This way, a mesoporous silica-based material functionalized with phosphine oxide groups was achieved [50].

The structure of the products obtained through the two-step synthesis were followed by vibrational spectra, in a DRIFT mode analysis, all spectra were analyzed by Kubelka-Munk equation, and normalized for better resolution minimizing scattering effects of the sample. Fig. 1 shows the comparison between the precursor HMS mesoporous material (black) the intermediate HMS-APTMS (red) and the final product HMS-CMPO (blue) spectra. The HMS material shows intense bands at 465(b), 800(s) and 1082(s) $cm^{-1}$  related to bending and stretching modes of the Si-O-Si bonds, as have been described before [53]. Also, medium intensity bands were observed at 1626, 3130 and 3430  $cm^{-1}$  related to -OH moieties over the surface of the material.

The Intermediate material HMS-APTMS (see Fig. 1) shows similar intense bands at 465(b), 800(s) and 1082(s) $cm^{-1}$  likewise the HMS. New lesser intense bands were observed at 698  $cm^{-1}$  related to primary amine wagging vibrational modes, 1318  $cm^{-1}$  related to C-N stretching and at 1491  $cm^{-1}$  related to the NH/CH scissoring as have been seen in APTES grafted over silica based mesoporous materials, at 1571  $cm^{-1}$  a new band related to NH stretching was observed, at 2873 and 2932  $cm^{-1}$  two bands related to  $CH_2$  and  $CH_3$  vibrational stretching were observed,

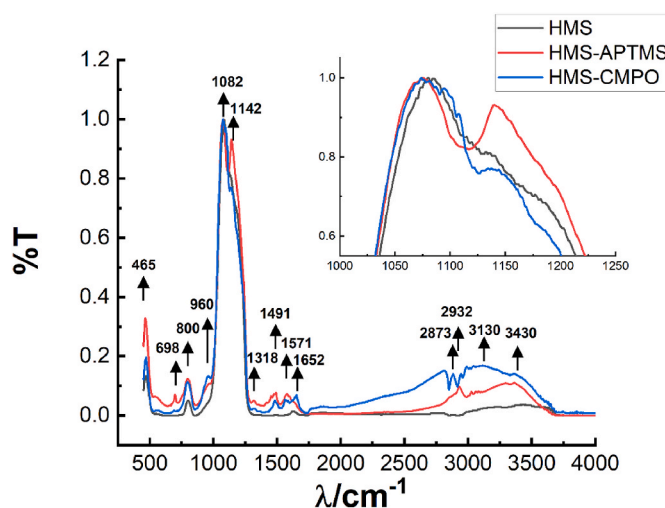


Fig. 1. DRIFT spectra of mesoporous materials, all spectra collected were analyzed by Kubelka-Munk function, and then normalized. HMS (black), HMS-APTMS (red) and HMS-CMPO (blue) samples were collected over the surface of a stainless-steel rod sampler. Between a range of 450-4000  $cm^{-1}$  wavelength. Inset a zoom to the 1000-1250  $cm^{-1}$  region.

$CH_3$  stretching may be due to free APTES moieties over the surface, as have been described before [50,54-57].

HMS-CMPO material vibrational spectra shows great resemblance with the HMS-APTES material one, a new band at 960  $cm^{-1}$  was observed related to P-O stretching, this band overlaps with a shoulder at 980  $cm^{-1}$  present in both HMS and HMS-APTMS material, that is related to Si-OH stretching [55,57], new bands are observed between 1095, 1491 and 1652 $cm^{-1}$ , where P-C stretching and P=O stretching have vibrational modes, as have been seen before in similar phosphine oxides structures [58].

In the inset of Fig. 1, the effect of the grafting may be seen clearly, where the HMS (black) show the band at 1082  $cm^{-1}$  associated with Si-O-Si vibrations, in the case of HMS-APTMS such band it is also presents but another intense band may be seen at 1142  $cm^{-1}$  in this region bands may be related to Si-O-C stretching [57], the case of the HMS-CMPO the band at 1142  $cm^{-1}$  is clearly smaller, and two additional shoulders may be seen around 1100 $cm^{-1}$ , related to P=O stretching of the CMPO moieties, overlapped with the band at 1082  $cm^{-1}$ . Bands at 2873 and 2932 $cm^{-1}$  were observed, in the region where  $CH_2$  and  $CH_3$  stretching may be found [50]. Further confirmation of the product was obtained by thermal gravimetric analyses and  $N_2$  adsorption/desorption isotherms.

### 3.2. Thermal stability characterization of mesoporous materials

Thermogravimetric analysis of the three mesoporous materials was carried out to determinate the thermal stability of the synthesized solids over 30° to 600 °C range. Fig. 2 shows the results obtained, where HMS (black square) shows higher stability, a small mass loss of 4 % was observed between 100 and 150 °C attributed to humidity present in the material. A smaller slope of mass loss was observed between 150 and 600 °C due to the slow dehydroxylation of the surface, as has been reported previously [50].

The Intermediate HMS-APTMS (red circles) shows three different slopes associated to a of mass loss, the first one between 100 and 150 °C attributed to a water loss (approximately 8 %) higher than HMS. The second one between 150 and 300 °C attributed to the slow degradation of the surface (2 % of mass loss), maybe due to some impurities of the synthesis and/or a slow dehydroxylation like the HMS. The third one between 300 and 600 °C attributed to degradation of the organic moiety of the surface by the modification with the N-(2-aminoethyl)-3-

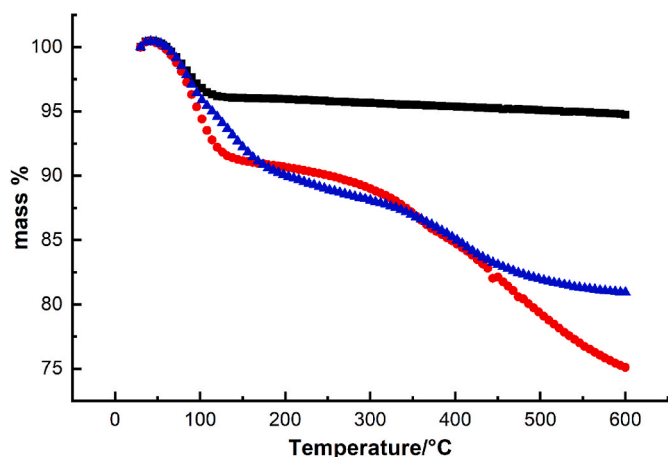


Fig. 2. Thermogravimetric analysis collected from samples of mesoporous materials HMS (black squares), APTMS (red circles) and CMPO (blue triangles). Between 30 and 600 °C, at 10 °C/min temperature rate.

aminopropyltrimethoxysilane. This time the mass loss was over 10 %. This mass amount is consistent with the amount of surface modification previously reported [50].

From Fig. 2 the thermal stability of the HMS-CMPO modified mesoporous material can be also observed (blue triangles), four different slopes may be observed in this case, the first one with a loss of about 10 % of mass between 100 and 150 °C attributed to the loss of water, as in the two cases before. The second one between 180 and 340 °C attributed to the slow degradation of the surface (3 % of mass loss), may be due to impurities of the synthesis and/or a slow dehydroxylation like the HMS-APTMS behavior. A third slope between 350 and 450 °C was observed with a mass loss of 5 % approximately, maybe due to a loss of carbamoyl methyl phosphine oxide moieties over surface, this mass loss starts at higher temperature compared with the observed with the HMS-APTMS, and its loss is smaller than the intermediate material, this may be due to a higher degradation temperature of the phosphine oxide moieties and to the lesser modification of the surface compared to the intermediate. The fourth slope observed between 450 and 600 °C shows again a slow mass loss (less than 2 %) with a similar ratio to the observed for the dehydroxylation process [50], first derivative of the TGA are provided in the supporting information (S1), where the difference between the degradation of the 3 solids may be observed as well.

### 3.3. Porosimetry of the mesoporous materials

The porosimetry of the mesoporous materials was characterized by N<sub>2</sub> Adsorption/Desorption isotherm analysis at 77K. All solids present similar hysteresis loop attributed to mesoporous material behavior, type IV hysteresis loop as IUPAC describes [59]. The matrix and condensation effects observed in Fig. 3 are consistent with mesoporous materials, in all the cases.

Nevertheless, significant differences may be observed between the synthesized materials, Porosimetry of the mesoporous materials were calculated by BET (Brauner, Emmett and Teller) equation method. Surface area, pore volume in the HMS-APTMS and HMS-CMPO decreased in comparison with HMS (see Table 1). In the other hand pore size is increased, this phenomenon is related to the obstruction of the smallest pores of the HMS-APTMS and HMS-CMPO materials due to the surface modification. BJH (Barrett-Joyner-Halenda) model was used to determinate pore size distribution, HMS material shows the smallest pores and higher contribution of the micropores and mesopores to the accumulative volume of the material (see Fig. S2 in supporting information). HMS-CMPO material presents a smaller pore size than HMS-APTMS material, also a higher contribution of the micropores and mesopores to the accumulative volume of the material in comparison

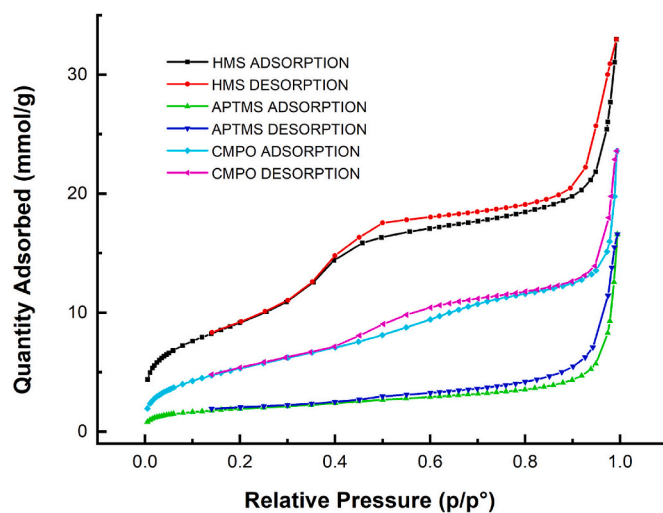


Fig. 3. Adsorption/Desorption isotherm of N<sub>2</sub> at 77K, collected from samples of mesoporous materials HMS (black/red), HMS-APTMS (magenta/cyan) and HMS-CMPO (green/blue). Between 0 and 1 relative pressure ratio.

Table 1

Porosity characteristic of the silica-based mesoporous materials obtained from BET method and BJH model.

Material	Average pore size [nm]	Pore volume [cm <sup>3</sup> /g]	Surface area [m <sup>2</sup> /g]
HMS	5.78	1.13	771
HMS-APTMS	13.16	0.54	157
HMS-CMPO	6.78	0.79	450

with APTMS (see Figs. S2–S3 in supporting information) this may be related to the interaction between the free APTMS with the grafted one, obstructing the smallest pores, which can be interpreted as a smaller surface area, and a broad pore size distribution than HMS and HMS-CMPO.

### 3.4. Crystallinity analysis of the mesoporous materials

Small-angle X-ray scattering (SAXS) of mesoporous materials were patterns of HMS and HMS-CMPO materials. Both profiles exhibit characteristic intense reflection at 2θ between 1.0° and 3.5° range was observed, this reflection centered at 2.0° which may be assigned to (1 0 0) crystalline plane, which is common in hexagonal mesoporous structures, as have been reported before [60–63]. HMS-CMPO material exhibits a lower reflection intensity, but still is clearly observed the plane reflection (Fig. 4). From these results the grafting of the CMPO over the surface of the HMS material present a small change in the crystallinity of the starting material due to chemical modification of the surface, the hexagonal structure within wormhole pores is still present.

#### 3.4.1. Electrochemical characterization of the modified electrode CPE-CMPO

An electrode of carbon paste modified with the mesoporous CMPO material was assembled by a mixture of carbon graphite powder (50% w/w), paraffin oil (30%w/w) and CMPO (20%w/w), this ratio was empirically optimized by using cyclic voltammetry (Fig. 5). The optimization was obtained from the analysis of the physical stability of the electrode, where swelling problems were observed when the concentration of the CMPO was over 20%w/w, this may be due to its hygroscopic behavior, as it was observed in the TGA analysis, where about 10 % of the weigh was water. All curves shows similar half wave potential ( $E_{1/2} = 224 \pm 2.8V$ ) which is calculated from the *semisum* of the anodic

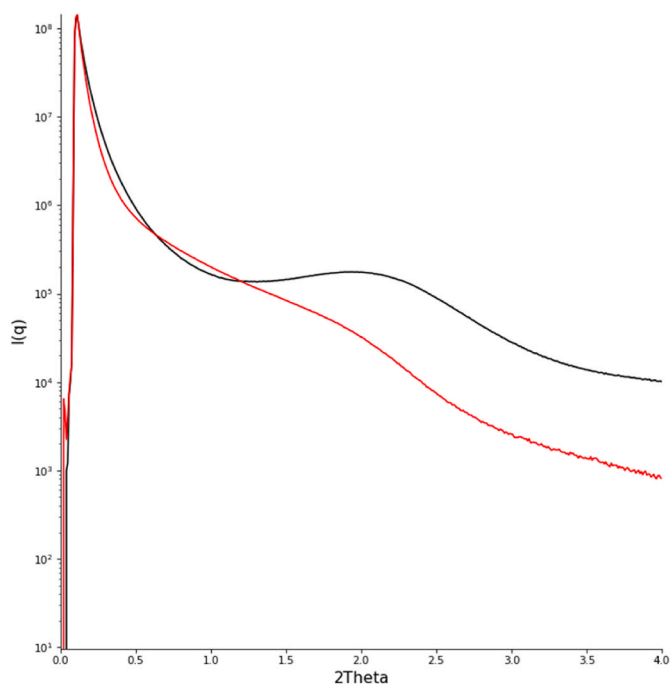


Fig. 4. XRD patterns obtained from HMS (black) and HMS-CMPO (red) materials.

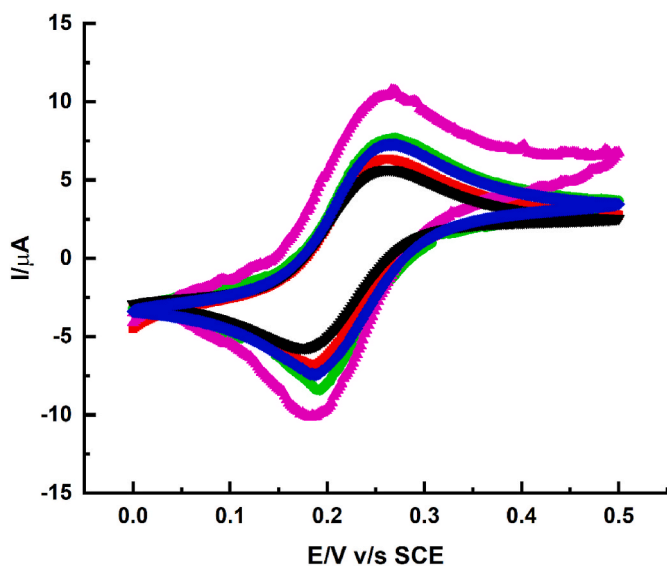


Fig. 5. Cyclic voltammetry obtained from aqueous solution of both  $K_3Fe(CN)_6$  and  $K_4Fe(CN)_6$  1 mM in KCl 1.0 M. The modified working electrode contains 0%w/w (black), 5%w/w (red), 10%w/w (blue), 15%w/w (green) and 20%w/w (purple) of CMPO material, reference electrode SCE, Pt wire as counter electrode. Scan rate  $5 \text{ mVs}^{-1}$ .

and cathodic potential peaks, this potential is an empirical approximation to the formal potential ( $E_f^0$ ) of the redox couple  $Fe(CN)_6^{4-}/Fe(CN)_6^{3-}$  defined in the Nernst equation, under empirical conditions and considering similar diffusion coefficient between both reactant and product species [64].

The CPE-CMPO modified electrodes shows a slightly higher anodic current response consistent with the increment of the CMPO modify ratio, this effect may be due to either an increase in the electroactive area of modified electrodes compared to the regular CPE (70%w/w graphite powder and 30%w/w paraffin oil) or may be due to a catalytic

effect over the redox probe  $Fe(CN)_6^{4-}/Fe(CN)_6^{3-}$ ; since this reaction is a well-known outer sphere reaction, non-catalytic effect is expected, and the values of  $E_{1/2}$  obtained are consistent with this hypothesis [64]. To evaluate the increase of the electroactive area of the modified electrodes the voltammograms obtained were analyzed by the Randles-Sevcik equation (1).

$$I_{PA} = 2.69 \cdot 10^5 \cdot n^{3/2} \cdot A \cdot C \cdot D^{1/2} \cdot \nu^{1/2} \quad (1)$$

Where  $I_{PA}$  is referred to the anodic current peak (Ampere),  $n$  is related to the number of electrons involved in the electrochemical reaction (1),  $A$  is the electroactive area ( $\text{cm}^2$ ),  $C$  is molar concentration of the active specie ( $0.000001 \text{ mol} \cdot \text{cm}^{-3}$ ),  $D$  is the diffusion coefficient of the  $Fe(CN)_6^{3-}$  ( $7.63 \cdot 10^{-6} \text{ cm}^2 \text{ s}^{-1}$ ) and  $\nu$  is the scan rate ( $0.005 \text{ V} \cdot \text{s}^{-1}$ ). [65].

The increase in the electroactive area due to the modifying CMPO material (see Table 2) shows a maximum at 20%w/w of the mesoporous material, this electrode presents an increment in the electroactive surface area for about 47 % compared to normal CPE electroactive area. This increase implies not only a higher surface due to a mesoporous material, but an increase in the electroactive sites over the surface of the electrode enhancing the electrode properties.

#### 3.4.2. CPE-CMPO electrode kinetics analysis

A kinetic analysis of the mechanism of mass transport to the surface of the electrode was performed by a scan rate study, evaluating the response of the electrode to a fast ( $200\text{--}1000 \text{ mVs}^{-1}$ ) and slow ( $5\text{--}100 \text{ mVs}^{-1}$ ) scan rate. A  $K_3Fe(CN)_6$  redox probe was used to study the electrode kinetics, where the ratio of the current against the scan rate (Fig. 6) shows an increase, and both anodic and cathodic peak potentials spreads away linearly with logarithm of the scan rate from 300 to 1000  $\text{mVs}^{-1}$  (supplementary S5), the nature of this behavior was studied by an analysis of the mass transport regime, where the current dependency with the scan rate was analyzed.

A linear behavior of the peak current against the square root scan rate plot (Fig. 6, inset A) shows a mass transport regimen ruled by diffusion, a slight difference may be observed between the cathodic (red dot) and anodic behavior (black dot), this may be due to the porosity of the material, which may influence the mass transport through the electrode surface, as have been seen before in material such as zeolites, where non Faradaic current due to the ions moving through the porosity of the material in the surface of the electrode occurs [49,66]. Nevertheless, both redox processes show higher resemblance with a diffusion than an adsorption ruled process. As the plot of peak current against scan rate (Fig. 6, Inset B) curve confirms this assumption.

#### 3.4.3. Electrochemical impedance spectroscopy study

Additionally, electrochemical Impedance Spectroscopy (EIS) analysis was used to determinate the effect of the concentration of the modification agent HMS-CMPO over the conductivity of the working electrode. Fig. 7 shows the spectrum obtained from the circuit assembled using the modified carbon paste electrodes, withing 0–20%w/w of CMPO, as working electrode, in an aqueous solution of 1 mM  $K_3Fe(CN)_6$  in 0.1 M  $NaNO_3$ . Ag/AgCl was used as reference electrode and a Pt wire as counter electrode.

The Nyquist plot obtained from the EIS analyses (Fig. 7) shows the behavior obtained from the electrochemical cell built with the carbon paste electrodes developed, as working electrode, with gradient of

Table 2

Electrochemical parameters extracted from Fig. 5.

Electrode	$I_{PA}$ [ $\mu\text{A}$ ]	$E_{1/2}$ [mV]	$-I_{PC}$ [ $\mu\text{A}$ ]	$A$ [ $\text{cm}^2$ ]
0%CMPO	7.90	0,220	7.89	0.151
5%CMPO	8.83	0,224	8.89	0.168
10%CMPO	9.50	0,226	9.93	0.181
15%CMPO	9.85	0,228	10.37	0.188
20%CMPO	11.62	0,222	13.61	0.222

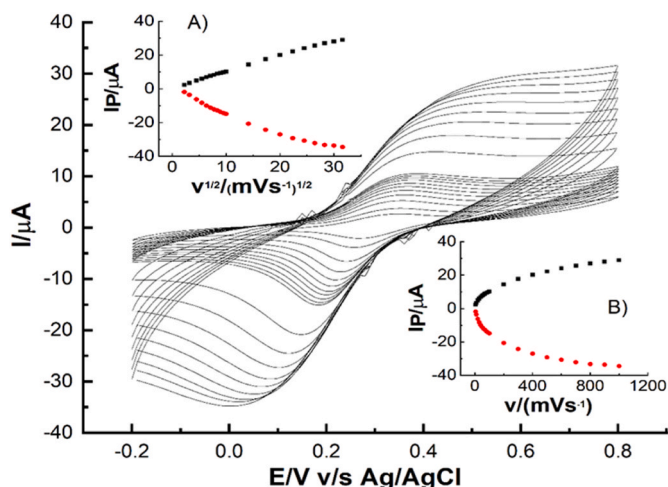


**Fig. 6.** Scan rate study, cyclic voltammograms were performed in a one chamber cell containing  $\text{K}_3\text{Fe}(\text{CN})_6$  1 mM in  $\text{NaNO}_3$  0.1 M aqueous solution. CPE-CMPO 20 % was used as working electrode, reference electrode Ag/AgCl, Pt wire as counter electrode. Scan rate used 1000 to 10  $\text{mVs}^{-1}$ . Inset A) Peak current against  $(I_p)$  square root scan rate plot ( $v^{1/2}$ ). Inset B) Peak current ( $I_p$ ) against scan rate plot ( $v$ ).

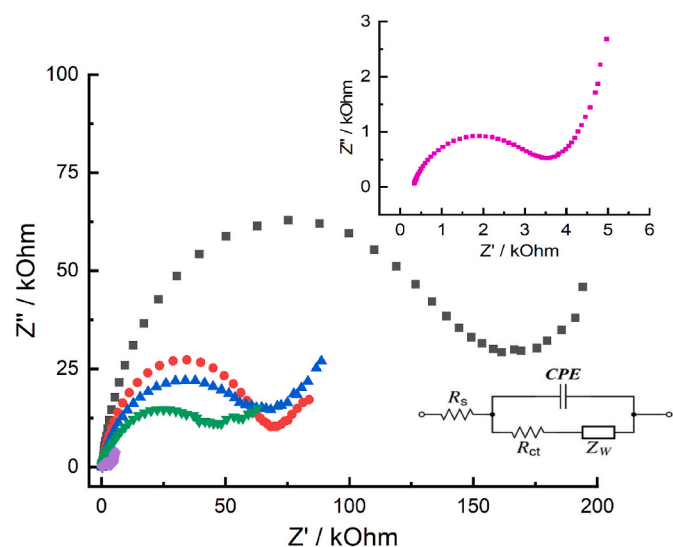


**Fig. 7.** Nyquist plot obtained from electrochemical impedance spectroscopy analysis, carried out over  $10^{-1}$  to  $10^5$  Hz, perturbation was set at 0.2V. Redox probe  $\text{Fe}(\text{CN})_6$  1 mM in 0.1 M  $\text{NaNO}_3$  aqueous solution. The modified contains, 0%w/w (black), 5%w/w (red), 10%w/w (blue), 15%w/w (green) and 20%w/w (purple) of HMS-CMPO. Reference electrode SCE and Pt wire as counter electrode. Inset a close view of 20%w/w CMPO modified electrode spectra.

composition from 0 to 20%w/w of HMS-CMPO. A classical Randles equivalent circuit was fitted to compare the collected spectrums, inset Fig. 6. A semicircle shaped behavior was observed at higher frequencies zone, attributed to an equivalent capacitor due to the ionic bilayer over the surface of the electrode generated over the polarization of the electrode through the experiment. This semicircle was followed by a  $45^\circ$  linear behavior, observed at lower frequencies, associated to the diffusion of the ionic species.

These spectrums were then fitted as an equivalent circuit represented by the Randles circuit model [7] (inset Fig. 7) were the circuit elements represent a resistance ( $R_s$ ), associated to the solution, a constant phase element (CPE) associated to the capacitor formed, which is affected by the porosity of the electrodes showing a smaller phase angle, (bode plots

Fig. S6), this behavior has been reported previously for carbon paste electrodes [49]. A second resistance ( $R_{CT}$ ) in parallel to the CPE was used to represent the resistance to the charge transfer of the electrode to the redox probe, then a Warburg impedance element  $Z_W$  was added in series to the  $R_{CT}$ , due to the diffusion of the redox probe.

From the fitted curves, a common origin around  $300\Omega$  was observed for all circuits associated to the solution resistance. The higher difference though, was observed in the second resistance ( $R_{CT}$ ) were the addition of CMPO to the electrode paste implies a massive decrease, from  $128.3\text{ k}\Omega$  to  $3.016\text{ k}\Omega$ , which is consistent with the enhance of the electroactive area detected in the scan rate study, this behavior over the modified carbon paste electrodes have been described before with different modifier agents such as Fe(II)-clinoptilolite nanoparticles, where the change observed in the Nyquist profiles are relatively similar [66].

Also Bode plots are provided as supporting information (Fig. S6), where at lower frequencies, the decrease of the impedance due to the decrease of the resistance to the charge transfer as the HMS-CMPO composition in the carbon paste increases from 0 to 20 %, may be observed clearly in the graph of  $|Z_w|$  against frequencies. The decrease observed in the  $-angle$  phase bode against the frequencies plot as the HMS-CMPO material composition increases, may be related to the increase of the porosity in the electrode surfaces, this inhomogeneities in the carbon paste electrode lower the angle associated to the capacitor element from approximately  $90^\circ$ – $60^\circ$  or even  $30^\circ$ , this behavior has been described for modified carbon paste electrodes before [48,49].

### 3.5. Electroadsorption-desorption study of $\text{La}^{3+}$ and $\text{Ce}^{3+}$

Electroadsorption-desorption studies were conducted to measure the amount of  $\text{La}^{3+}$  and  $\text{Ce}^{3+}$  that may be extracted from aqueous solution using the mesoporous silica functionalized with carbamoyl methyl phosphine oxide (CMPO) as modification agent (20%w/w) in the carbon paste mixture to fabricate a carbon paste working electrode (CMPO-CPE). These experiments were performed in two steps, the first one consists of the electroadsorption process, where applying a controlled reduction potential of  $-0.6\text{V}$  over 100s in a Chronoamperometric program, the experiment was performed in a 20 mL one chamber electrochemical cell, using three electrodes setup, where Ag/AgCl electrode was used as reference and Pt wire as counter electrode.

The electrochemical cell was filled with 18 mL of 50 ppm  $\text{La}^{3+}$  or  $\text{Ce}^{3+}$  in a 0.1 M of  $\text{NaNO}_3$  aqueous solution, inert Ar atmosphere was controlled for avoidance of oxygen interference. The optimization for the adsorption pH was developed in previous works [50], for  $\text{La}^{3+}$  pH 5.0 was optimal and for  $\text{Ce}^{3+}$  pH 6.0. Under these conditions the adsorption of the trivalent species to the HMS-CMPO material occurs without any potential applied [50].

In the other hand, when the electrode surface was polarized by the negative potential applied, the migration of both lanthanides was increased, which was consistent with the increase in the charge registered, the cathodic potential applied in both cases was  $-0.6\text{V}$ , this potential increased the charge associated to migration, avoiding further electrochemical reaction. Under pH range between 4.0 and 6.0 the formation of insoluble hydroxylated species of  $\text{La}^{3+}$  starts [67], when overpotential is applied to  $\text{La}^{3+}$  under pH 5.0, the mono and dihydroxylated lanthanum species migrated to the electrode surface and electroadsorption occurs. In the other hand,  $\text{Ce}^{3+}$  hydroxylated species stay soluble between pH 7.0–8.0 [68]. This phenomenon supports the electroadsorption method proposed.

Then a reduction potential is applied to regenerate the surface of the electrode. This process was empirically defined also, by the increase of the current registered using an oxidation program, applying  $+0.2\text{V}$  by 100s after the reduction program. The current increase observed in the experiment (see Fig. 8) was attributed to desorption of trivalent species.

To corroborate the above hypothesis, the second step of the study, the desorption process, was design including another technique,

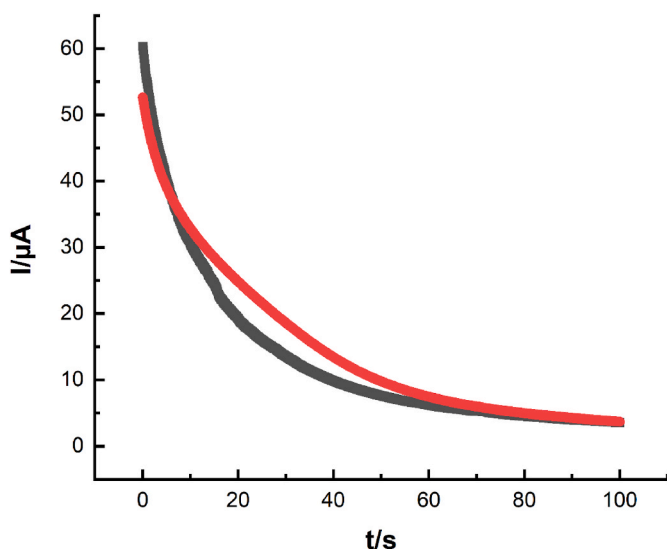


**Fig. 8.** Chronoamperometry desorption curves, obtained after a pretreatment of 100s at  $-0.6\text{V}$  under pH 5.0 for 10 ppm  $\text{La}^{3+}$ , and pH 6.0 for 10 ppm  $\text{Ce}^{3+}$  both in 0.1 M  $\text{NaNO}_3$  aqueous solution. The electrochemical cell was set up by a working electrode 20%CMPO CPE, Ag/AgCl as reference electrode, and Pt wire as counter electrode.

Inductively Coupled Plasma Atomic Emission Spectrophotometry (ICP-AES), which allows to quantify the amount of  $\text{La}^{3+}$  and  $\text{Ce}^{3+}$  extracted from adsorption process and then redissolved into a second desorption solution. The desorption experiment was performed in a secondary electrochemical cell filled with 2 mL of 0.1 M of  $\text{NaNO}_3$ , pH was adjusted to 2.0 for desorption process, under this condition  $\text{La}^{3+}$  and  $\text{Ce}^{3+}$  was found totally diluted, and oxo-hydroxyl complexes species should not be found [67–69].

This design allows us to avoid the misleading effect of the water splitting and pH variation through the desorption process, which has been reported in similar experiments. After the desorption process 1 mL of the solution was diluted to 10 mL of  $\text{NaNO}_3$  0.1 M solution, acidified with  $\text{HNO}_3$  65 %, a blank solution and a solution of a mixture 1 ppm  $\text{La}^{3+}/\text{Ce}^{3+}$  was also analyzed for every sample measured, to corroborate the results.

The results of the desorption experiments are summarized in Table 3, where the amount mass of  $\text{La}^{3+}$  shows higher extracted ratio, it was calculated taken the concentration of the sample and extrapolating it to the amount of mass extracted from the absorption solution. The mass calculated for  $\text{La}^{3+}$  was 74  $\mu\text{g}$  over 10 adsorption/desorption cycles, against the 15  $\mu\text{g}$  obtained for  $\text{Ce}^{3+}$  over 10 adsorption/desorption cycles. These results (see Table 4) may be due to a higher affinity of the electrode for the  $\text{La}^{3+}$  species over  $\text{Ce}^{3+}$ , which is very interesting, since the charge density of both cations is quite similar, this phenomenon may be also explained due to the presence of oxo-hydroxyl complexes form at pH 6.0 with the  $\text{La}^{3+}$  as has been reported previously [67–69].

Anyway, to determine selectivity of one species over the other, further experiments need to be done to evaluate this method in a more relevant environment. The stability of the electrodes was checked by measuring changes in current using cyclic voltammetry previous and after the electroadsorption/desorption cycles (supplementary material S7), the changes in current were measured and were below 1 % after every cycle tested.

#### 4. Conclusions

A hexagonal like mesoporous silica material was functionalized with oxide phosphine moieties, to develop a CMPO material with higher adsorption properties for  $\text{La}^{3+}$  and  $\text{Ce}^{3+}$ , this solid porosimetry was fully characterized, presenting high surface area and small pore size. The

**Table 3**

Electrochemical parameters extracted from EIS fitted curves.

Electrode	$R_s$ [ $\Omega$ ]	CPE [ $\mu\text{F}$ ]	$Z_w$ [ $\mu\text{F}$ ]	$R_{CT}$ [ $\text{k}\Omega$ ]	%Error
0%CMPO	347.7	0.181	34.73	128.3	>5 %
5%CMPO	296.2	0.345	12.24	65.91	>5 %
10%CMPO	293.9	0.285	25.52	58.04	>5 %
15%CMPO	261.2	0.884	14.96	42.16	>5 %
20%CMPO	280.2	1.473	2.180	3.016	>5 %

**Table 4**

Inductively Coupled Plasma Atomic Emission Spectrophotometry results, blank solution containing  $\text{NaNO}_3$  0.1 M and pH 2, desorption solutions were collected after 10 cycles of adsorption/desorption of  $\text{La}^{3+}$  and  $\text{Ce}^{3+}$ .

Solution	$[\text{La}^{3+}]$ $\text{mgL}^{-1}$	$[\text{Ce}^{3+}]$ mg $\text{L}^{-1}$	Mass $\text{La}^{3+}$ $\mu\text{g}$	Mass $\text{Ce}^{3+}$ $\mu\text{g}$
Blank	<0.1	<0.1	N/A	N/A
1ppm $\text{La}^{3+}$ +1 ppm $\text{Ce}^{3+}$	1.10	1.15	110	115
Desorption $\text{La}^{3+}$	0.74	<0.1	74	N/A
Desorption $\text{Ce}^{3+}$	<0.1	0.15	N/A	15

CMPO material presents higher hygroscopicity compared to HMS and thermal stability until 340  $^\circ\text{C}$  where degradation of the functional groups was observed.

Electrochemical properties of the CMPO functionalized material were studied using this solid as component of carbon paste electrodes, the porosity and functional groups present in the CMPO generated an increase in both electroactive area and the conductivity of the electrode developed. The hygroscopicity of the CMPO material limited the amount of this material in the carbon paste mixture to 20%w/w, since at higher concentration the electrode starts to swell, losing physical stability.

No redox couples attributed to CMPO reactions were observed between the electrochemical window studied ( $-0.6$  to  $1.0\text{V}$ ), this electrode presented suitable properties for its use as electroadsorption surface for  $\text{La}^{3+}$  and  $\text{Ce}^{3+}$ . The electroadsorption-desorption studies were used to develop a method for extraction of the lanthanides showing higher extractant capacity of the method for  $\text{La}^{3+}$ , by 47 % over the amount  $\text{Ce}^{3+}$ . Electrodes does not present higher changes in current after electroadsorption/desorption experiments, even after 100 cycles. These results suggest a selective extraction of  $\text{La}^{3+}$  over  $\text{Ce}^{3+}$ , to calculate the selectivity for  $\text{La}^{3+}$  from the ion mixture additional studies must be designed, nevertheless, these preliminary results are a promising start to develop a method for selective electroadsorption of lanthanides.

#### CRedit authorship contribution statement

**Carlos Díaz:** Writing – original draft, Methodology, Investigation, Formal analysis, Conceptualization. **Mauricio Gómez:** Visualization, Resources. **Alicia Matta:** Visualization, Validation. **Jaime Pizarro:** Writing – review & editing, Validation, Supervision, Resources, Conceptualization.

#### Declaration of competing interest

The authors declare that they have no known competing financial interests or personal relationships that could have appeared to influence the work reported in this paper.

#### Data availability

Data will be made available on request.

## Acknowledgements

Authors acknowledge financial support from the projects: USA2055\_DICYT University of Santiago de Chile. Project USA1799 Vridei 091912JP\_GO University of Santiago de Chile. Dicyt grant N° 092112 PK, Fondef Grant ID1810229, Proyecto ANID FONDECYT postdoctorado N3220359. Proyecto ANID FONDECYT postdoctorado N3210179.

## Appendix A. Supplementary data

Supplementary data to this article can be found online at <https://doi.org/10.1016/j.micromeso.2024.113248>.

## References

- R.A. Bellezoni, A.P. Adeogun, M.X. Paes, J.A.P. de Oliveira, Tackling climate change through circular economy in cities, *J. Clean. Prod.* 381 (2022), <https://doi.org/10.1016/j.jclepro.2022.135126>.
- F. Taghizadeh-Hesary, K. Dong, C. Zhao, H. Phoumin, Can financial and economic means accelerate renewable energy growth in the climate change era? The case of China, *Econ. Anal. Pol.* 78 (2023) 730–743, <https://doi.org/10.1016/j.eap.2023.04.013>.
- G. Curran, Coal, climate and change: the narrative drivers of Australia's coal economy, *Energy Res. Social Sci.* 74 (2021), <https://doi.org/10.1016/j.erss.2021.101955>.
- Q. Guo, W. You, A comprehensive evaluation of the international competitiveness of strategic minerals in China, Australia, Russia and India: the case of rare earths, *Resour. Pol.* 85 (2023), <https://doi.org/10.1016/j.resourpol.2023.103821>.
- J. Shuai, X. Peng, Y. Zhao, Y. Wang, W. Xu, J. Cheng, Y. Lu, J. Wang, A dynamic evaluation on the international competitiveness of China's rare earth products: an industrial chain and tech-innovation perspective, *Resour. Pol.* 75 (2022), <https://doi.org/10.1016/j.resourpol.2021.102444>.
- J.Y. Kang, W. Ha, Y.P. Shi, Magnetic N-rich carbon nitride framework material for the high selectivity extraction and determination of La(III), *Talanta* 225 (2021), <https://doi.org/10.1016/j.talanta.2021.122086>.
- M. Zhang, W. Li, J. Zhao, M. Chen, Comparative study of the effects of CaO and Ce-La mixed metal on the microstructure and properties of AZ91 alloy, *J. Mater. Res. Technol.* 9 (2020) 5194–5203, <https://doi.org/10.1016/j.jmrt.2020.03.036>.
- I.M. Ali, E.S. Zakaria, M. Khalil, A. El-tantawy, F.A. El-Saied, Efficient enrichment of Eu<sup>3+</sup>, Tb<sup>3+</sup>, La<sup>3+</sup> and Sm<sup>3+</sup> on a double core shell nano composite based silica, *J. Inorg. Organomet. Polym. Mater.* 30 (2020) 1537–1552, <https://doi.org/10.1007/s10904-019-01303-z>.
- R. Pattanaik, S. Mishra, Impact of operating variables on the extraction efficiency of [THAH]+[DEHP]- in solvent extraction of La(III), *Mater. Today Proc.* 67 (2022) 1283–1289, <https://doi.org/10.1016/j.matpr.2022.09.076>.
- C. Cristiani, E.M. Iannicelli-Zubiani, M. Bellotto, G. Dotelli, E. Finocchio, S. Latorrata, G. Ramis, P. Gallo Stampino, Capture and release mechanism of lan ions by new polyamine-based organoclays: A model system for rare-earths recovery in urban mining process, *J. Environ. Chem. Eng.* 9 (2021), <https://doi.org/10.1016/j.jece.2020.104730>.
- J. Shuai, X. Peng, Y. Zhao, Y. Wang, W. Xu, J. Cheng, Y. Lu, J. Wang, A dynamic evaluation on the international competitiveness of China's rare earth products: an industrial chain and tech-innovation perspective, *Resour. Pol.* 75 (2022), <https://doi.org/10.1016/j.resourpol.2021.102444>.
- W. Wang, E. Li, Z. Peng, C. Guo, S. Hou, Q. Li, Flotation separation of bastnaesite from monazite using depressant dextrin hydrate and its depression mechanism, *Miner. Eng.* 200 (2023), <https://doi.org/10.1016/j.mineng.2023.108151>.
- V.N. Tirtom, A. Dinçer, S. Becerik, T. Aydemir, A. Çelik, Comparative adsorption of Ni(II) and Cd(II) ions on epichlorohydrin crosslinked chitosan-clay composite beads in aqueous solution, *Chem. Eng. J.* 197 (2012) 379–386, <https://doi.org/10.1016/j.cej.2012.05.059>.
- Z. Zhu, A. Zheng, Fast determination of yttrium and rare earth elements in seawater by inductively coupled plasma-mass spectrometry after online flow injection pretreatment, *Molecules* 23 (2018), <https://doi.org/10.3390/molecules23020489>.
- Determination of Lanthanum and Rare Earth Elements, (n.d.).
- S. Qin, H. Bin, Q. Yongchao, R. Wanjuan, J. Zucheng, Determination of trace rare earth impurities in high-purity cerium oxide by using electrothermal vaporization ICP-AES after HPLC separation with 2-ethylhexyl hydrogen 2-ethylhexylphosphonate resin as the stationary phase, *J. Anal. At Spectrom* 15 (2000) 1413–1416, <https://doi.org/10.1039/b003107k>.
- X.-Q. Shan, J. Lian, B. Wen, Effect of organic acids on adsorption and desorption of rare earth elements, n.d. [www.elsevier.com/locate/chemosphere](http://www.elsevier.com/locate/chemosphere).
- X. Tan, X. Wang, M. Fang, C. Chen, Sorption and desorption of Th(IV) on nanoparticles of anatase studied by batch and spectroscopy methods, *Colloids Surf. A Physicochem. Eng. Asp.* 296 (2007) 109–116, <https://doi.org/10.1016/j.colsurfa.2006.09.032>.
- Z. Tu, Z. Hu, X. Chang, L. Zhang, Q. He, J. Shi, R. Gao, Silica gel modified with 1-(2-aminoethyl)-3-phenylurea for selective solid-phase extraction and preconcentration of Sc(III) from environmental samples, *Talanta* 80 (2010) 1205–1209, <https://doi.org/10.1016/j.talanta.2009.09.009>.
- X. Wang, C. Chen, J. Du, X. Tan, D. Xu, S. Yu, Effect of pH and aging time on the kinetic dissociation of 243Am(III) from humic acid-coated  $\gamma$ -Al<sub>2</sub>O<sub>3</sub>: a chelating resin exchange study, *Environ. Sci. Technol.* 39 (2005) 7084–7088, <https://doi.org/10.1021/es0506307>.
- M. Ismael, Environmental remediation and sustainable energy generation via photocatalytic technology using rare earth metals modified g-C<sub>3</sub>N<sub>4</sub>: a review, *J. Alloys Compd.* 931 (2023), <https://doi.org/10.1016/j.jallcom.2022.167469>.
- S.A. Cotton, J.M. Harrowfield, Lanthanides: coordination chemistry, in: *Encyclopedia of Inorganic and Bioinorganic Chemistry*, John Wiley & Sons, Ltd, 2012, <https://doi.org/10.1002/9781119951438.eibc2062>.
- K.L. Nash, A Review of the Basic Chemistry and Recent Developments in Trivalent F-Elements Separations, Solvent Extraction and Ion Exchange, 11, 1993, pp. 729–768, <https://doi.org/10.1080/07366299308918184>.
- C.W. Noack, K.M. Perkins, J.C. Callura, N.R. Washburn, D.A. Dzubak, A. K. Karamalidis, Effects of ligand chemistry and geometry on rare earth element partitioning from saline solutions to functionalized adsorbents, *ACS Sustain. Chem. Eng.* 4 (2016) 6115–6124, <https://doi.org/10.1021/acssuschemeng.6b01549>.
- F. Xie, T.A. Zhang, D. Dreisinger, F. Doyle, A critical review on solvent extraction of rare earths from aqueous solutions, *Miner. Eng.* 56 (2014) 10–28, <https://doi.org/10.1016/j.mineng.2013.10.021>.
- J.C. Callura, Ligand-functionalized adsorbents for the extraction and recovery of rare earth elements, Carnegie Mellon University, Pittsburgh, Thesis degree of doctor of Philosophy in Civil and Environmental Engineering, 2018, <https://doi.org/10.1184/R1/7212371.v1>.
- D.L. Ramasamy, E. Repo, V. Srivastava, M. Sillanpää, Chemically immobilized and physically adsorbed PAN/acetylacetone modified mesoporous silica for the recovery of rare earth elements from the waste water-comparative and optimization study, *Water Res.* 114 (2017) 264–276, <https://doi.org/10.1016/j.watres.2017.02.045>.
- T. Kegl, A. Košak, A. Lobnik, Z. Novak, A.K. Kralj, I. Ban, Adsorption of rare earth metals from wastewater by nanomaterials: a review, *J. Hazard Mater.* 386 (2020), <https://doi.org/10.1016/j.jhazmat.2019.121632>.
- M. Mao, T. Yan, J. Shen, J. Zhang, D. Zhang, Capacitive removal of heavy metal ions from wastewater via an electro-Adsorption and electro-reaction coupling process, *Environ. Sci. Technol.* 55 (2021) 3333–3340, <https://doi.org/10.1021/acs.est.0c07849>.
- C. Zhao, L. Zhang, R. Ge, A. Zhang, C. Zhang, X. Chen, Treatment of low-level Cu (II) wastewater and regeneration through a novel capacitive deionization-electrodeionization (CDI-EDI) technology, *Chemosphere* 217 (2019) 763–772, <https://doi.org/10.1016/j.chemosphere.2018.11.071>.
- J. Landon, X. Gao, A. Omosebi, K. Liu, Progress and outlook for capacitive deionization technology, *Curr Opin Chem Eng* 25 (2019) 1–8, <https://doi.org/10.1016/j.coche.2019.06.006>.
- X. Zhao, H. Wei, H. Zhao, Y. Wang, N. Tang, Electrode materials for capacitive deionization: a review, *J. Electroanal. Chem.* 873 (2020) 114416, <https://doi.org/10.1016/j.jelechem.2020.114416>.
- R. Chen, T. Sheehan, J.L. Ng, M. Brucks, X. Su, Capacitive deionization and electrosorption for heavy metal removal, *Environ. Sci.* 6 (2020) 258–282, <https://doi.org/10.1039/c9ew00945k>.
- A.S. Yasin, I.M.A. Mohamed, M.T. Amen, N.A.M. Barakat, C.H. Park, C.S. Kim, Incorporating zirconia nanoparticles into activated carbon as electrode material for capacitive deionization, *J. Alloys Compd.* 772 (2019) 1079–1087, <https://doi.org/10.1016/j.jallcom.2018.09.057>.
- H. Zhang, P. Liang, Y. Bian, Y. Jiang, X. Sun, C. Zhang, X. Huang, F. Wei, Moderately oxidized graphene-carbon nanotubes hybrid for high performance capacitive deionization, *RSC Adv.* 6 (2016) 58907–58915, <https://doi.org/10.1039/c6ra10088k>.
- S. Bao, J. Duan, Y. Zhang, Recovery of V(V) from complex vanadium solution using capacitive deionization (CDI) with resin/carbon composite electrode, *Chemosphere* 208 (2018) 14–20, <https://doi.org/10.1016/j.chemosphere.2018.05.149>.
- R. Cao, J. Zhang, D. Wang, F. Sun, N. Li, J. Li, Electrodeposition cobalt sulfide nanosheet on laser-induced graphene as capacitive deionization electrodes for uranium adsorption, *Chem. Eng. J.* 461 (2023) 142080, <https://doi.org/10.1016/J.CEJ.2023.142080>.
- H. Afsharara, E. Asadian, B. Mostafiz, K. Banan, S.A. Bigdeli, D. Hatamabadi, A. Keshavarz, C.M. Hussain, R. Keçili, F. Ghorbani-Bidkorpheh, Molecularly imprinted polymer-modified carbon paste electrodes (MIP-CPE): a review on sensitive electrochemical sensors for pharmaceutical determinations, *TRAC, Trends Anal. Chem.* 160 (2023), <https://doi.org/10.1016/j.trac.2023.116949>.
- L. Ahmadpour-Mobarakeh, A. Nezamzadeh-Ejhieh, A zeolite modified carbon paste electrode as useful sensor for voltammetric determination of acetaminophen, *Mater. Sci. Eng. C* 49 (2015) 493–499, <https://doi.org/10.1016/j.msec.2015.01.028>.
- T. Tamiji, A. Nezamzadeh-Ejhieh, Sensitive voltammetric determination of bromate by using ion-exchange property of a Sn(II)-clinoptilolite-modified carbon paste electrode, *J. Solid State Electrochem.* 23 (2019) 143–157, <https://doi.org/10.1007/s10008-018-4119-4>.
- Z. Arham, F.B. Awad, T. Nakai, I. Ismaun, L. Anhusadar, Modification of nickel slag nanomaterials as a smart modifier of carbon paste electrodes in voltammetry-based lead pollutant detection, *Mater. Chem. Phys.* 309 (2023), <https://doi.org/10.1016/j.matchemphys.2023.128419>.

- [42] Z. Yang, Voltammetry for quantitative determination of trace mercury ions in water via acetylene black modified carbon paste electrode, *Alex. Eng. J.* 87 (2024) 107–113, <https://doi.org/10.1016/j.aej.2023.12.007>.
- [43] Q. Song, Y. Liu, L. Zhang, Z. Xu, Selective electrochemical extraction of copper from multi-metal e-waste leaching solution and its enhanced recovery mechanism, *J. Hazard Mater.* 407 (2021), <https://doi.org/10.1016/j.jhazmat.2020.124799>.
- [44] X. Yang, L. Liu, W. Tan, C. Liu, Z. Dang, G. Qiu, Remediation of heavy metal contaminated soils by organic acid extraction and electrochemical adsorption, *Environ. Pollut.* 264 (2020), <https://doi.org/10.1016/j.envpol.2020.114745>.
- [45] Z. Song, Y. Chen, N. Ren, X. Duan, Recent advances in the fixed-electrode capacitive deionization (CDI): innovations in electrode materials and applications, *Environ. Functional Mater.* (2023), <https://doi.org/10.1016/j.efmat.2023.11.001>.
- [46] A. Ahmadi, A. Nezamzadeh-Ejhi, A comprehensive study on electrocatalytic current of urea oxidation by modified carbon paste electrode with Ni(II)-clinoptilolite nanoparticles: experimental design by response surface methodology, *J. Electroanal. Chem.* 801 (2017) 328–337, <https://doi.org/10.1016/j.jelechem.2017.08.009>.
- [47] A. Nezamzadeh-Ejhi, N. Masoudipour, Application of a new potentiometric method for determination of phosphate based on a surfactant-modified zeolite carbon-paste electrode (SMZ-CPE), *Anal. Chim. Acta* 658 (2010) 68–74, <https://doi.org/10.1016/j.aca.2009.10.064>.
- [48] F. Fuenzalida, D. Aravena, C. García, M. García, R. Arce, G. Ramírez, C. Díaz, M. Isaacs, M. del C. Arévalo, M.J. Aguirre, Effect of the substituent of the cation of N-octylpyridinium hexafluorophosphate in the electrical and electrochemical response of carbon paste electrodes modified with these ionic liquids, *Electrochim. Acta* 258 (2017) 959–969, <https://doi.org/10.1016/j.electacta.2017.11.147>.
- [49] C. Díaz, C. García, P. Iturriaga-Vásquez, M.J. Aguirre, J.P. Muenra, R. Contreras, R. Ormazábal-Toledo, M. Isaacs, Experimental and theoretical study on the oxidation mechanism of dopamine in n-octyl pyridinium based ionic liquids-carbon paste modified electrodes, *Electrochim. Acta* (2013), <https://doi.org/10.1016/j.electacta.2013.08.103>.
- [50] Claudia Andrea Ortiz Calderón, Jaime Francisco Pizarro Konczak, Ximena Andrea Castillo Castillo, Mauricio Manuel Gómez Barrena, Carlos Patricio Díaz Navarro, RENÉ Andre garrido lazo, proceso DE obtencion de una matriz mesoporosa tipo HMS funcionalizada para la adsorción selectiva de La+3 Y Ce+3, Matriz Mesoporosa Y SU USO Para La Adsorción Selectiva DE Lantano Y Cerio (2021) 202003459. <https://ion.inapi.cl/Patente/ConsultaAvanzadaPatentes.aspx>. (Accessed 31 July 2023).
- [51] W. Cai, L. Tan, J. Yu, M. Jaroniec, X. Liu, B. Cheng, F. Verpoort, Synthesis of amino-functionalized mesoporous alumina with enhanced affinity towards Cr(VI) and CO<sub>2</sub>, *Chem. Eng. J.* 239 (2014) 207–215, <https://doi.org/10.1016/j.cej.2013.11.011>.
- [52] M. Gómez, J. Pizarro, X. Castillo, A. Ghisolfi, C. Díaz, M. de Lourdes Chávez, D. Cazorla-Amorós, Development of mesoporous materials from biomass ash with future applications as adsorbent materials, *Microporous Mesoporous Mater.* 299 (2020), <https://doi.org/10.1016/j.micromeso.2020.110085>.
- [53] A.G. Gebretatos, F. Banat, T. Witoon, C.K. Cheng, Synthesis of sustainable rice husk ash-derived nickel-decorated MCM-41 and SBA-15 mesoporous silica materials for hydrogen storage, *Int. J. Hydrogen Energy* 51 (2024) 255–266, <https://doi.org/10.1016/j.ijhydene.2023.11.154>.
- [54] R.G. Acres, A.V. Ellis, J. Alvin, C.E. Lenahan, D.A. Khodakov, G.F. Metha, G. Andersson, Molecular structure of 3-aminopropyltriethoxysilane layers formed on silanol-terminated silicon surfaces, *J. Phys. Chem. C* 116 (2012) 6289–6297, <https://doi.org/10.1021/jp212056s>.
- [55] V. Ivanovski, M. Bukleski, M. Madalska, E. Hey-Hawkins, Vibrational spectra of a ferrocenyl phosphine derivative chemisorbed on 3-aminopropylsilyl modified silica gel, *Vib. Spectrosc.* 69 (2013) 57–64, <https://doi.org/10.1016/j.vibspec.2013.09.009>.
- [56] Z. Rahmatpanah, M.M. Alavi Nikje, Synthesis and characterization of thermally stable polyurea-TiO<sub>2</sub> nanocomposites based on amine terminated polybutadiene, *Polym. Bull.* 80 (2023) 2437–2455, <https://doi.org/10.1007/s00289-022-04132-2>.
- [57] R.M. Pasternack, S.R. Amy, Y.J. Chabal, Attachment of 3-(aminopropyl) triethoxysilane on silicon oxide surfaces: dependence on solution temperature, *Langmuir* 24 (2008) 12963–12971, <https://doi.org/10.1021/la8024827>.
- [58] C. Kizilkaya, M. Biçen, S. Karataş, A. Güngör, Thermal, mechanical and structural investigation of copolyimide-silica hybrids containing phosphine oxide, *Prog. Org. Coating* 86 (2015) 108–116, <https://doi.org/10.1016/j.porgcoat.2015.04.019>.
- [59] F. Sotomayor, A.P. Quantatec, F.J. Sotomayor, K.A. Cychoz, M. Thommes, Characterization of micro/mesoporous materials by physisorption: concepts and case studies. <https://www.researchgate.net/publication/331260891>, 2018.
- [60] S. Yousatit, H. Pitayachinchot, A. Wijitrat, S. Chaowamalee, S. Nuntang, S. Soontaranon, S. Rugmai, T. Yokoi, C. Ngamcharussrivichai, Natural rubber as a renewable carbon source for mesoporous carbon/silica nanocomposites, *Sci. Rep.* 10 (2020), <https://doi.org/10.1038/s41598-020-69963-3>.
- [61] A. Zhang, S. Jiang, X. Shan, J. Wang, M. Zhou, M. Chai, Hollow mesoporous silica by ion exchange-induced etching strategy for high temperature proton exchange membrane, *Front. Energy Res.* 9 (2021), <https://doi.org/10.3389/fenrg.2021.741806>.
- [62] L. López-Pérez, M.A. López-Martínez, K. Djanashvili, K. Góra-Marek, K.A. Tarach, M.E. Borges, I. Melián-Cabrera, Process intensification of mesoporous material's synthesis by microwave-assisted surfactant removal, *ACS Sustain. Chem. Eng.* 8 (2020) 16814–16822, <https://doi.org/10.1021/acsschemeng.0c05438>.
- [63] Y. Yin, W. Deng, H. Wang, A. Li, C. Wang, Z. Jiang, H. Wu, Fabrication of hybrid membranes by incorporating acid-base pair functionalized hollow mesoporous silica for enhanced proton conductivity, *J Mater Chem A Mater* 3 (2015) 16079–16088, <https://doi.org/10.1039/c5ta03276h>.
- [64] A.J. Bard, L.R. Faulkner, *Electrochemical Methods : Fundamentals and Applications*, Wiley, 2001. <https://www.wiley.com/en-us/Electrochemical+Methods%3A+Fundamentals+and+Applications%2C+2nd+Edition-p-9780471043720>. (Accessed 30 January 2018).
- [65] C. Báez, F. Navarro, F. Fuenzalida, M.J. Aguirre, M.C. Arévalo, M. Afonso, C. García, G. Ramírez, J.A. Palenzuela, Electrical and electrochemical behavior of carbon paste electrodes modified with ionic liquids based in N-octylpyridinium bis (trifluoromethylsulfonyl)imide. A theoretical and experimental study, *Molecules* 24 (2019), <https://doi.org/10.3390/molecules24183382>.
- [66] M. Nosuhi, A. Nezamzadeh-Ejhi, High catalytic activity of Fe(II)-clinoptilolite nanoparticles for indirect voltammetric determination of dichromate: experimental design by response surface methodology (RSM), *Electrochim. Acta* 223 (2017) 47–62, <https://doi.org/10.1016/j.electacta.2016.12.011>.
- [67] S. Iftekhar, D.L. Ramasamy, V. Srivastava, M.B. Asif, M. Sillanpää, Understanding the factors affecting the adsorption of Lanthanum using different adsorbents: a critical review, *Chemosphere* 204 (2018) 413–430, <https://doi.org/10.1016/j.chemosphere.2018.04.053>.
- [68] L.F. Arenas, C. Ponce De León, F.C. Walsh, Electrochemical redox processes involving soluble cerium species, *Electrochim. Acta* 205 (2016) 226–247, <https://doi.org/10.1016/j.electacta.2016.04.062>.
- [69] M. Mucci, G. Douglas, M. Lüring, Lanthanum modified bentonite behaviour and efficiency in adsorbing phosphate in saline waters, *Chemosphere* 249 (2020), <https://doi.org/10.1016/j.chemosphere.2020.126131>.